

## OPEN Intense laser interaction with micro-bars

Michal Elkind<sup>1,2</sup>, Itamar Cohen<sup>1,2</sup>, David Blackman<sup>3</sup>, Talia Meir<sup>1,2,4</sup>, Lior Perelmuter<sup>1,2</sup>, Tomer Catabi<sup>1,2</sup>, Assaf Levanon<sup>1,2</sup>, Siegfried H. Glenzer<sup>5</sup>, Alexey V. Arefiev<sup>3</sup> & Ishay Pomerantz<sup>1,2</sup>✉

Intense laser fields interact very differently with micrometric rough surfaces than with flat objects. The interaction features high laser energy absorption and increased emission of MeV electrons, ions, and of hard x-rays. In this work, we irradiated isolated, translationally-symmetric objects in the form of micrometric Au bars. The interaction resulted in the emission of two forward-directed electron jets having a small opening angle, a narrow energy spread in the MeV range, and a positive angle to energy correlation. Our numerical simulations show that following ionization, those electrons that are pulled into vacuum near the object's edge, remain in-phase with the laser pulse for long enough so that the Lorentz force they experience drive them around the object's edge. After these electrons pass the object, they form attosecond duration bunches and interact with the laser field over large distances in vacuum in confined volumes that trap and accelerate them within a narrow range of momentum. The selectivity in energy of the interaction, its directionality, and the preservation of the attosecond duration of the electron bunches over large distances, offer new means for designing future laser-based light sources.

The interaction of intense laser fields with matter at its sharp interface with the vacuum is central to understanding phenomena like energy absorption of intense light in matter<sup>1</sup>, emission of coherent soft X-ray radiation from irradiated polished surfaces<sup>2</sup>, and formation of sheath fields responsible for MeV ion emission from irradiated thin foils<sup>3</sup>. Following ionization, the laser fields near the interface, which are enhanced by diffraction, extract electrons from the plasma<sup>4</sup>. At these intensities, the magnetic and electric terms of the Lorentz force become comparable, and the so-called  $J \times B$  heating mechanism participates in transferring laser energy to the electrons<sup>5</sup>.

After half an optical cycle as the laser field changes direction, these electrons would be pushed back. If the irradiated object is sufficiently large, the electron trajectories are likely to drive them back into the plasma, where their energy will be dissipated through collisions. This is the basis for the vacuum heating (VH) model<sup>1</sup> which predicts the energy transfer of laser light to flat surfaces and its sensitivity to the laser's polarization and angle of incidence<sup>6</sup>.

In the case of *rough* surfaces, a range of experiments have shown diverse emission features when the irradiated objects possessed geometric structures with dimensions on the order of the laser wavelength or smaller. These include the irradiation of surfaces coated with nanowires<sup>7–10</sup>, micrometric scale pillars<sup>11–13</sup>, plastic spheres<sup>14–16</sup>, water droplets<sup>17</sup>, and modulated “grating” targets irradiated at incidence angles close to the resonant condition for surface plasmon excitation<sup>18,19</sup>. Compared to the irradiation of flat surfaces, these objects present higher ionization level<sup>10</sup>, increased laser absorption<sup>8,16</sup>, volumetric heating into ultrahot plasma<sup>20</sup> and high-energy X-ray emission<sup>7,13,14,17</sup>, as well as the emission of MeV electrons<sup>11,13</sup>, protons<sup>12,15,16</sup>, and fusion neutrons<sup>9</sup>.

Proposed explanations for these features include local enhancement of the electromagnetic fields<sup>11,12</sup>, multi-pass stochastic heating of electrons through Mie resonance<sup>14</sup>, and an increased number of possible trajectories that enable electrons to undergo efficient VH<sup>13,15</sup>.

In those experiments, the stochastic nature of the targets' geometric features along with the typical laser's pointing instability, raise substantial uncertainty about the illuminated structure details.

Clearly *isolated* micrometric targets with well-defined geometries better serve the purpose of understanding the reaction mechanism. In the particular case of targets which are circularly symmetric in the laser's polarization plane, the interaction is readily analyzed in the framework of Mie theory<sup>21</sup>. One such numerical investigation

<sup>1</sup>The School of Physics and Astronomy, Tel Aviv University, 69978 Tel Aviv, Israel. <sup>2</sup>Center for Light-Matter Interaction, Tel Aviv University, 69978 Tel Aviv, Israel. <sup>3</sup>Department of Mechanical and Aerospace Engineering, University of California San Diego, La Jolla, CA 92093, USA. <sup>4</sup>The School of Electrical Engineering, Tel Aviv University, 69978 Tel Aviv, Israel. <sup>5</sup>SLAC National Accelerator Laboratory, Menlo Park, CA 94025, USA. ✉email: ipom@tauex.tau.ac.il

for the case of irradiated He droplets<sup>4</sup> revealed that enhancement of the local field at the target surface ejects electrons with MeV-level energies into vacuum. The interaction results in two jets comprised of attosecond-duration electron bunches emitted at certain angles set by the ratio of the droplet radius to the wavelength and the ratio of the plasma frequency to the laser frequency. The authors noted that the angular distribution of the emitted ions follows the predicted Mie angles better than that of the electrons. They attributed this feature to modifications in the electrons direction as they move away from the droplet. These modifications will be discussed in the work presented here.

The emission of these two electron jets was first observed experimentally by Cardenas et al.<sup>22</sup> who irradiated the tips of W needles with laser intensities in the range of  $a_0 = 0.2\text{--}5.3$ , where  $a_0$  is the normalized laser intensity which for a laser pulse of wavelength  $\lambda$  is given in practical units by  $a_0 = 0.86\lambda [\mu\text{m}] \sqrt{I [10^{18} \text{ Wcm}^{-2}]}$ . Unstable laser pointing combined with the 3D geometry of the conically-shaped targets resulted in an unknown effective irradiation area<sup>23</sup>. Nevertheless, under the assumption that Mie scattering governs the emission, the authors were able to infer the effective target radius of each shot from the opening angle between the electron jets, and found it to be insensitive to the laser intensity. Mie scattering would not account for the observed multi-MeV electron energies, which the authors attributed to subsequent interaction with the laser fields in vacuum<sup>24</sup>.

To understand how intense light couples to wavelength-scale formations, we irradiated (see Methods) single micrometric Au bars ("micro-bars") with a rectangular cross-section of ( $w = 2.0\text{--}6.0 \mu\text{m}$ , perpendicular to the beam direction)  $x$  ( $d = 0.2 \mu\text{m}$ , along the beam direction), which were completely immersed in the focal volume of an intense laser field, as illustrated in Fig. 1. The figure shows a comparison of the measured energy spectra of electrons emitted from these micro-bars, along the laser direction, when positioned perpendicular ("p-polarization") or parallel ("s-polarization") to the laser's electric field, as well as for irradiation of an Au foil of the same thickness. The increased yields and coupling of laser energy to high-energy electrons is clearly observed in the case of a micro-bar irradiated in p-polarization.

Figure 2 shows angle-resolved energy spectra of electrons emitted from  $w = 2\text{--}6 \mu\text{m}$  wide micro-bars, following irradiation by a p-polarized,  $a_0 = 2.7$  laser pulse. Microscope images of each of the micro-bars prior to irradiation, which also feature the laser spot in low power, are shown for each case. Two lobes of high-energy

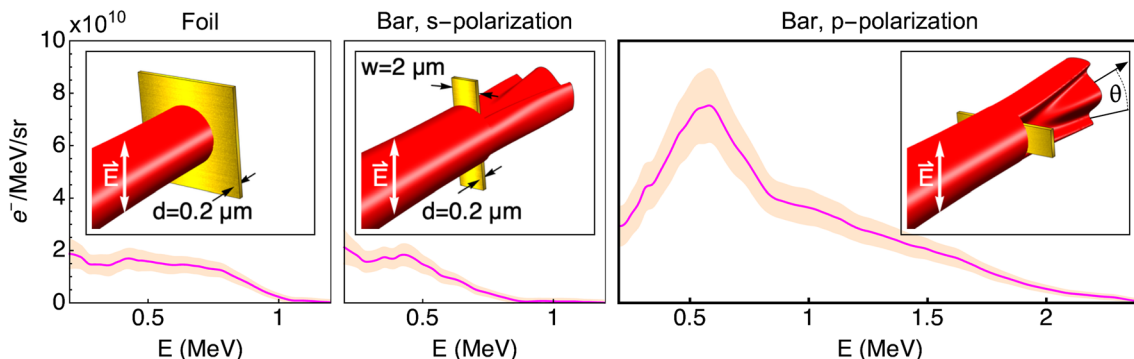


**Figure 1.** Measured spectra of electrons emitted from  $d = 0.2 \mu\text{m}$  thick Au targets under irradiation with a relativistic laser pulse ( $a_0 = 2.7$ ) in three configurations: a flat foil which is much wider than the focal spot size; a  $w = 2.0 \mu\text{m}$  wide bar in s-polarization (bar is parallel to  $\vec{E}$ ); and a bar with the same dimensions irradiated in p-polarization.

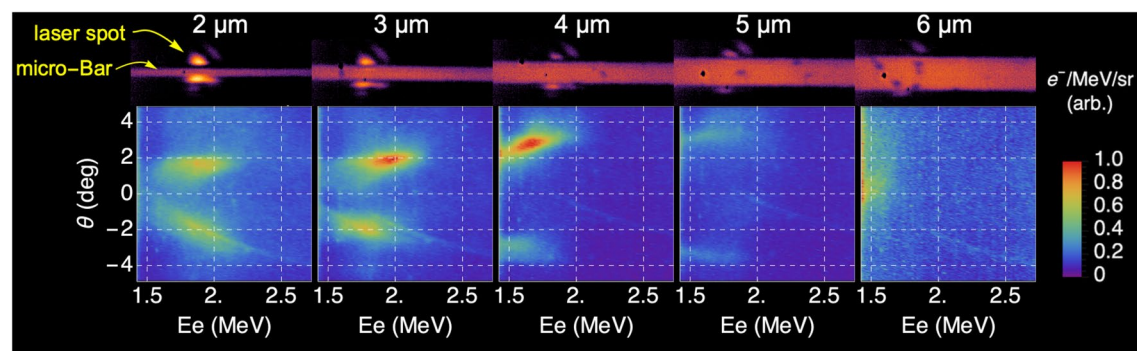


**Figure 2.** Measured angle-resolved spectra of electrons emitted from Au micro-bars, irradiated with an intense laser pulse ( $a_0 = 2.7$ ) in p-polarization. The angle  $\theta$  is defined to be in the polarization plane of the electric field, as indicated in Fig. 1. The micro-bars are all  $d = 0.2 \mu\text{m}$  thick, and their width, in the range of  $w = 2\text{--}6 \mu\text{m}$ , is indicated on top. Also shown are microscope images of the micro-bars, with 10x magnification, featuring the laser spot in low power prior to irradiation.

electrons, with a low separation angle ( $< 4^\circ$ ) are observed around the bar's symmetry axis. These electrons are confined to a narrow energy range and present a positive angle-to-energy correlation. As the width of the micro-bar approaches the focal spot size, the emission angle increases while the number of electrons falls. The shot-to-shot variability in the relative intensity of the two jets  $|I_{Left}-I_{Right}|/(I_{Left}+I_{Right})$  is found to have a mean value of 9.5%. This variability is attributed to the laser's pointing instability, which was measured to be  $0.43 \mu\text{m}$  (RMS). We note that the same asymmetry between the two electron lobes can also arise from the random phase of the sub-cycle emission process when using *few-cycle* laser pulses<sup>22</sup>.

The underlying dynamics was revealed through particle-in-cell (PIC) simulations using the EPOCH code<sup>25</sup> (see the Methods section for details). Figure 3a shows a snapshot from a 3D PIC simulation for a  $w = 2 \mu\text{m}$  wide micro-bar irradiated with a p-polarized  $a_0 = 4.6$  laser pulse. The snapshot was taken at  $t = 0$ , when the peak of the laser field impinged on the micro-bar, i.e., time of maximum electron emission. The transverse component of the laser field is shown in a red-to-blue color scale. Superimposing the emitted electrons on Fig. 3a, with their energy density distribution shown in green, clearly shows a double-jet formation comprised of attosecond electron bunches spanning over about four optical cycles.

A confirmation that indeed the emission of high-energy electrons is a consequence of the micrometric dimensions of the micro-bar is given in Fig. 3b, in which 2D PIC results for an extended target (top) and a  $w = 1.0 \mu\text{m}$  wide micro-bar (bottom) in otherwise identical conditions are compared. The density of high-energy electrons ( $> 1 \text{ MeV}$ ) is shown in green, and is observed only for the micro-bar case. See Supplementary Video 1 for the full animation of this simulation.

The origin for these high-energy electron bunches is identified by following the Lorentz forces they experience. Figure 3c shows four simulation snapshots taken within the duration of a single optical cycle following the peak of the interaction, under the same conditions as in Fig. 3b. The longitudinal ( $E_x$ ) and transverse ( $E_y$ ) components of the electric field and the out-of-plane magnetic field ( $B_z$ ) are shown with red-to-blue color scales. The density of high-energy ( $E > 1 \text{ MeV}$ ) electrons is shown in green. Due to diffraction, the field amplitudes close to the target edge reach values up to 2.1 times higher than the laser's field. The forces exerted by each of the field components on one electron bunch are indicated with white arrows.  $E_x$  pulls and pushes electrons within each half optical cycle, in synchronization with  $E_y$ , which accelerates them in alternating directions. Therefore at each half cycle, electrons emerging close to one of the edges of the micro-bar are pushed in a trajectory beyond the extent of the target. Between  $t = 0$  and  $t = 0.4\text{T}$ , the relativistic electron bunch overlaps with the same half-optical-cycle. Thus, the out-of-plane magnetic field introduces a  $v \times B$  motion which rotates the bunch around the object's corner. In the VH model for extended objects, the transverse motion of the electrons has no effect on the energy absorption, and the analysis is often conducted in a reference frame boosted in the transverse direction,

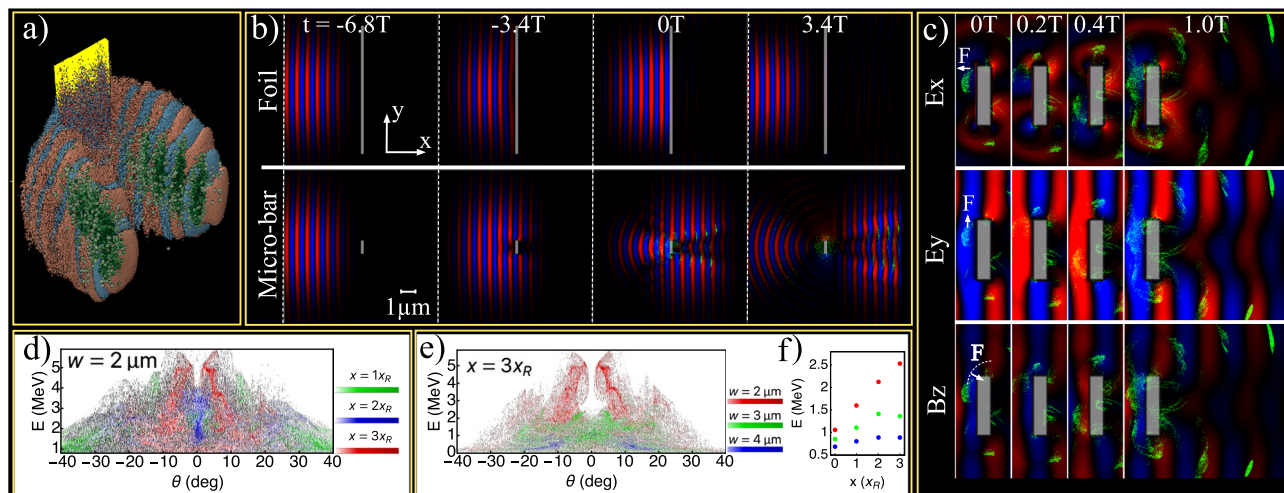


**Figure 3.** PIC simulation results. (a) A snapshot from a 3D-PIC simulation taken at  $t = 0$ , when the peak of a p-polarized  $a_0 = 4.6$  laser field, impinges on the micro-bar. The transverse component of the electric field ( $E_y$ ) is shown in a red-to-blue color scale. The density of electrons having energy above a threshold of 1 MeV is shown in green. (b) Four snapshots of two 2D-PIC simulations for the irradiation of  $0.2 \mu\text{m}$  thick targets: a  $w = 10.0 \mu\text{m}$  wide foil (top) and a  $w = 1.0 \mu\text{m}$  wide micro-bar (bottom). Both simulations ran in otherwise identical conditions, and the color scales are the same as in (a). (c) Four snapshots from a 2D-PIC simulation taken over one optical cycle at  $0 < t < 1\text{T}$ . The blue-to-red color scales indicate the field strength of the electric field in the longitudinal ( $E_x$ ) and transverse ( $E_y$ ) directions, and of the out-of-plane magnetic field ( $B_z$ ), each at a different arbitrary self-normalized scale. The Lorentz force exerted by each of the field components on one example electron bunch is indicated by white arrows. (d) Three snapshots of angle-resolved electron energy spectra for irradiation of a  $w = 2.0 \mu\text{m}$  wide micro-bar, taken after a propagation distance of 1 (green), 2 (blue), and 3 (red) Rayleigh ranges. (e) Three snapshots of angle-resolved electron energy spectra taken after a propagation distance of  $3x_R$ , for the cases of  $w = 2.0 \mu\text{m}$  (red),  $w = 3.0 \mu\text{m}$  (blue), and  $w = 4.0 \mu\text{m}$  (green) wide micro-bars. The PIC simulations in (d) and (e) were performed with the actual laser intensity of the experiments ( $a_0 = 2.7$ ). (f) Average electron energy at  $t = 0$ , and after propagation of 1, 2, and 3 Rayleigh ranges.

so that only a 1D longitudinal motion remains<sup>2</sup>. Since the electron emission is in the electric field polarization plane<sup>4</sup>, the same description also applies to electrons emitted from a micro-bar irradiated in s-polarization (Fig. 1, middle), where the electron trajectories are parallel to the long dimension of the micro-bar. But in p-polarization, when the target posses micrometric features, the combined effect of  $E_y$  and  $B_z$  may push electrons around the target. This is the origin of the two-lobe formation observed in the experiment.

We now turn to the interaction of the bunched electrons with the diffracted laser fields while propagating over a long distance in vacuum. Three snapshots of angle-resolved electron spectra are shown in Fig. 3d, taken after propagation distances of 1 (green), 2 (blue), and 3 (red) Rayleigh ranges ( $x_R$ ). Even at these large distances, some electrons continue to accelerate while maintaining a low divergence angle. At  $3x_R$ , the highest energy electrons ( $E > 5$  MeV) present a positive angle-to-energy correlation, as observed in the experiment. Another experimental observation that is recreated in the PIC (Fig. 3e) concerns the diminishing electron energies and the increase in the emission angle for wider micro-bars. The overall higher electron energies observed in the simulations compared to the experiment, are typical to 2D numeric effects<sup>26</sup>.

The average energy of the electron bunches at their peak emission time, and following their propagation over 1, 2, and 3 Rayleigh ranges is plotted in Fig. 3f, with the same color coding of Fig. 3e. At the time of emission, the electron energy is found to decrease linearly with  $w$ , i.e. with the square root of the focal intensity distribution. This is consistent with the energy scaling of electrons oscillating in the transverse laser field<sup>27</sup> typically observed for intensities above  $10^{18}$  Wcm<sup>-2</sup>. Due to the reduction of the transmitted laser fields, the average energy of electrons emitted from a  $w = 4\ \mu\text{m}$  bar is increased by only 30% after propagation of  $3x_R$ , while for a  $w = 2\ \mu\text{m}$  target their energy is more than doubled.

Following the electrons over a long propagation distance using PIC is impractical because of heavy computational load, hence the low statistics of high-energy electrons in Figs. 3d, e. However, since the bunching of hot electrons observed in Fig. 3 indicates that the space charge forces between them are small, we are able to use a “particle pusher” type simulation to study the single electron interaction with the diffracted laser beam over a long distance, in a parametric manner.

The transverse component of a Gaussian laser field is given by

$$E_y^G(y, x, t; w_0) = E_0 \frac{w_0}{w} \exp \left\{ -y^2/w^2 + i(kx - \arctan(x/x_R) + ky^2/(2R_c) - \omega t) \right\} \quad (1)$$

where the beam waist radius  $w(x) = w_0 \sqrt{1 + (x/x_R)^2}$  is set by its value at focus  $w_0$  and its Rayleigh range  $x_R = \pi w_0^2/\lambda$ , and where the radius of curvature is given by  $R_c(x) = x + x_R^2/x$ . The transverse and longitudinal fields of the diffracted beam, obscured by the micro-bar, are then given by<sup>28</sup>:

$$E_y = E_y^G(y, x, t; w_{beam}) - E_y^G(y, x, t; w_{bar}), \quad E_x = E_y \frac{y \cdot \cos(\arctan(y/x))}{q_0 + x} \quad (2)$$

with  $q_0 = \frac{i\pi w_0^2}{\lambda}$ . The trajectories of electrons interacting with these fields having a set initial position and momentum at time  $t = 0$ , may be followed using a finite difference method:

$$\Delta \vec{p} = -e(\vec{E} + \vec{\beta} \times \vec{B})\Delta t \quad \rightarrow \quad \vec{p}(t + \Delta t) = \vec{p} + \Delta \vec{p} \quad \rightarrow \quad \vec{x}(t + \Delta t) = \vec{x} + \frac{\vec{p}}{\gamma m} \Delta t \quad (3)$$

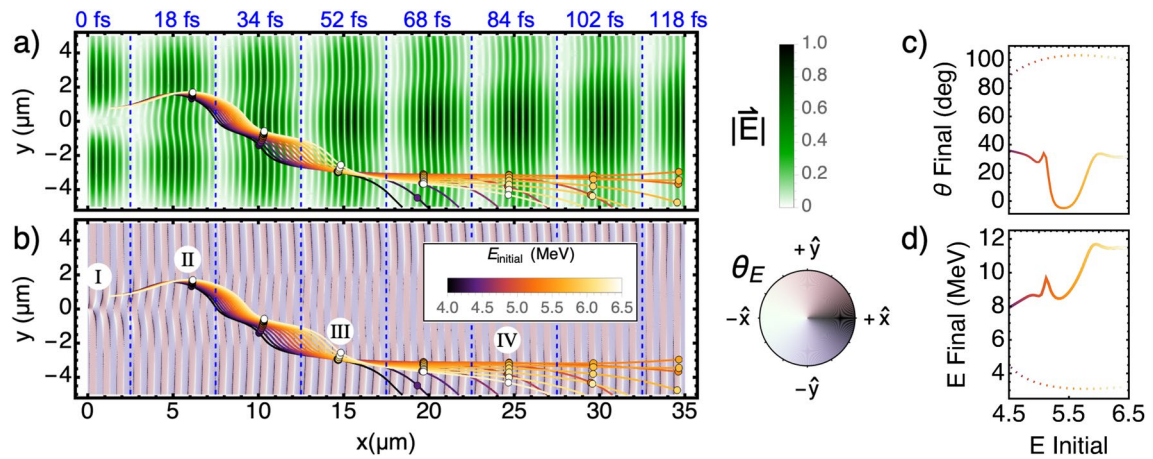
where  $\gamma = \sqrt{1 + p^2/(mc^2)}$  and  $\beta = |p|/\gamma mc$ .

Figure 4 presents simulated trajectories of electrons interacting with the diffracted field in vacuum. The electric field's magnitude (Fig. 4a) and direction (Fig. 4b) are plotted on eight temporal snapshots at equal intervals, starting at  $t = 0$ , where the peak intensity of the pulse is incident on a  $w = 2\ \mu\text{m}$  wide micro-bar positioned at  $x = 0$ . See Supplementary Video 2 for the full animation. The annular low-field channel formed in the diffracted field is clearly observed in Fig. 4a. The white slivers in Fig. 4b indicate regions in which an electron would be accelerated forward. These are the regions in which electrons are observed to be bunching in the PIC results (Fig. 3), therefore they served as the injection point (labeled ①) in this simulation.

The simulated trajectories of electrons initially moving forward with energies in the range of 4–6.5 MeV are overlaid on Fig. 4a, b. Their location at the time of each snapshot is indicated with a circle. While propagating forward, the electrons dephase with respect to the laser's optical cycle according to their velocity. Between ① and ②, the forward-pushing regions of the field are tilted with respect to  $x$ , so the electrons disperse transversely by different amounts according to the amount of their dephasing. At the shadow of the micro-bar ( $-w/2 < y < w/2$ ), the forward-pushing regions are observed to diminish as  $x$  approaches  $x_R$ , thus between ② and ③ the electrons are expelled outward and slip back by two optical cycles, until they are trapped again in another white sliver, on the negative side of the  $y$  axis.

As  $x$  approaches  $x_R$ , the overall curvature of the diffracted field flattens. At ④ only electrons of a narrow energy range, which settled at the center of the low field channel, are observed to be pushed forward, while slower or faster electrons are expelled by the transverse forces at the edges of the channel.

The final emission angle and energy are plotted in Fig. 4c, d as a function of the initial electron energy in a solid line with a color scale that matches their trajectories in Fig. 4a, b. The trapping of electrons of a narrow energy range, the overall net acceleration, and the positive angle-to-energy correlation that were observed in the experiment and PIC, are also featured here. Electron bunches injected with the same initial conditions into a Gaussian laser pulse unobscured by a micro-bar, are quickly expelled outward, as is observed by the dotted lines in Fig. 4c, d.



**Figure 4.** Simulation of electrons propagating in the diffracted laser field. Shown are eight snapshots of the electric field magnitude (a) and its direction (b), captured at equal intervals during the propagation of the pulse over one Rayleigh length ( $x_R = 34.7 \mu\text{m}$ ). The trajectories of electrons, injected at ① with initial energies in the range of 4–6.5 MeV, are overlaid in (a,b). The positions of the electrons at each time frame are marked with circles. (c) and (d) show the final emission angle and energy (solid curves), respectively, as a function of the initial electron energy. The color of the curve matches that of the trajectories in (a,b). Simulation results for electrons injected at the same initial position propagating under a Gaussian field (i.e. without a micro-bar) is indicated by dotted lines.

In conclusion, by irradiating single micrometric scale Au bars we revealed new features of how intense laser fields couple to wave-length scale objects. The physical process takes place in two steps: first, electrons that were pulled into vacuum near the edge of the target circumvent the cold material by the pull of the transverse electric field and the  $v \times B$  motion under the laser's magnetic field. This dynamics repeats at the peak of the field's intensity every half-optical cycle, and results in a train of attosecond duration bunches of electrons. After passing the target, the diffracted laser fields interact with the electrons in vacuum over a distance of many Rayleigh ranges. The electrons bunch in small confined volumes in which the diffraction field pushes them forward, keeping them nearly in-phase with the laser pulse. But the structure of these volumes changes along the propagation direction, making this a highly selective process. The electrons that manage to stay in phase are accelerated and emitted in the form of two forward-directed jets ( $\theta < 4^\circ$ ) comprised of attosecond duration bunches, while the rest are expelled by the transverse field. These emission characteristics motivate the use of such isolated micrometric target for generating short-wavelength radiation with attosecond pulse durations through Thomson scattering with a counter-propagating laser pulse or by seeding a free-electron laser<sup>22</sup>.

## Methods

### Target fabrication

The targets were free-standing Au bars suspended over rectangular openings in a 250  $\mu\text{m}$  thick Si wafer support. The fabrication process starts with a Si wafer pre-coated on its front with a 200-nm thick layer of high-stress  $\text{Si}_3\text{N}_4$ . The back side of the wafer is spin-coated with layers of resist (MicroChem SF9) and photoresist (Micro-Chem AZ-1518), on which 3.0 mm  $\times$  0.4 mm rectangular gaps are photolithographed. The Si is then etched in a 30% KOH solution at 90°C. The process spontaneously stops when the inner surface of the front side  $\text{Si}_3\text{N}_4$  is exposed. Next, the  $\text{Si}_3\text{N}_4$  side of the wafer is spin-coated with layers of the same resist and photoresist. 2–6  $\mu\text{m}$  wide rectangular openings, which would form the micro-bars, are photolithographed over the gaps. The wafer is coated with a 10-nm thick Ti adhesion layer and a 190-nm thick layer of Au. The  $\text{Si}_3\text{N}_4$  around the bars is removed by reactive ion etching and immersion in Acetone. Finally, the remaining  $\text{Si}_3\text{N}_4$  layer below the Au bars is removed by dry-etching.

### PIC simulation

We used the fully relativistic EPOCH PIC code<sup>25</sup> to carry out the simulations. One simulation was conducted in 3D, with minimal temporal and spatial resolutions and covering a brief duration, and four 2D simulations (with  $w = 1, 2, 3$ , and 4  $\mu\text{m}$ ) to follow the trajectories of the emitted electrons over a significant distance in vacuum. In both cases, the laser pulse exhibited a Gaussian temporal profile with a width of 30 fs (FWHM) and a wavelength of 800 nm, at p-polarization. The laser beam was focused to a Gaussian intensity distribution with a radius of 3.5  $\mu\text{m}$  (FWHM), yielding peak laser intensity of  $a_0 = 4.6$ . The PIC simulations in Fig. 3d and e were performed with the actual laser intensity of the experiments,  $a_0 = 2.7$ .

The 3D simulation space was defined as a  $(6 \mu\text{m})^3$  box divided into  $(100)^3$  computational mesh cells. The 2D simulation space was defined as a  $(18 \mu\text{m})_\perp \times (30 \mu\text{m})_\parallel$  box with  $(6144)_\perp \times (6144)_\parallel$  computational mesh cells. Here  $\perp$  and  $\parallel$  are with respect to the laser propagation direction. The 2D simulations ran for 40 fs, after which the simulation box was set to move in the laser propagation direction at the speed of light, for additional 350 fs.

The targets were representative of electrons, protons, and singly-ionized Au ions. Their initial distribution was rectangular, of  $(2\text{--}6 \mu\text{m})_\perp \times (0.2 \mu\text{m})_\parallel$ , with a uniform density of 3000 times the plasma's critical density,

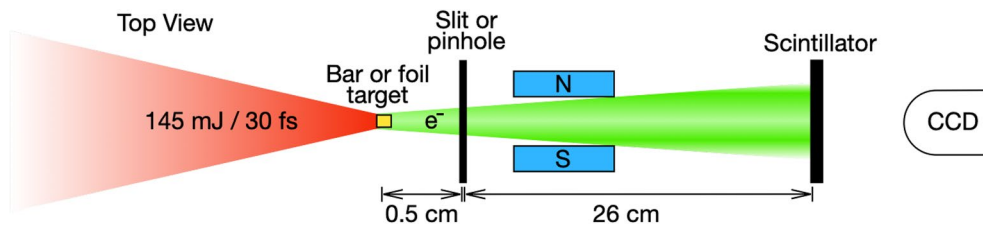


**Figure 5.** Top-view cartoon drawing of the experimental setup (elements are not to-scale). The long dimension of the micro-bar is out-of-plane. See text for details.

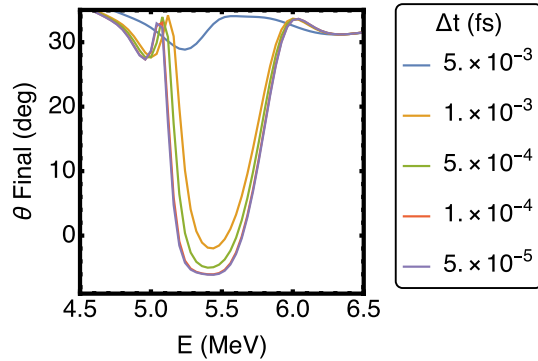


**Figure 6.** The final emission angles of electrons simulated with the Particle Pusher simulation code. Numerical stability of the code is achieved for  $\Delta t < 5 \times 10^{-4}$  fs.

and a density exponential gradient around them with a scale length of 13.3-nm ( $\lambda / 60$ ). For the 3D simulation, this density profile was extruded over the third direction to 10  $\mu\text{m}$ .

### Experimental setup

We performed the experiments using the NePTUN 20 TW laser system at Tel Aviv University<sup>29</sup>. Figure 5 shows cartoon schematics of the experimental setup. 30-fs long laser pulses with energies of 145 mJ (on-target) and pulse contrast better than  $10^{130}$ , were focused using an f/2.5 off-axis parabolic mirror unto the Au bar targets. We measured 70% of the laser energy to be contained within a circle of 3.5  $\mu\text{m}$  diameter.

We recorded electron spectra using a charge-coupled device imaging a CsI(Tl) scintillator<sup>31</sup> at the focal plane of magnetic spectrometers. We used two configurations to generate the spectrograms shown in Figs. 1 and 2: (1) An acceptance of  $\Omega = 0.12$  msr and  $0.2 < E_e < 4.2$  MeV, as described in detail in the Supp. note of Ref.<sup>32</sup>, but with a reduced magnetic field of 0.25 T. The scintillator was covered on its target-facing side with a 15- $\mu\text{m}$  thick aluminum foil to block scattered light. (2) A wide angular acceptance spectrometer of  $\theta = 182$  mrad and  $0.9 < E_e < 6$  MeV, which consisted of a 1.7 cm (horizontal)  $\times$  400  $\mu\text{m}$  (vertical) wide slit followed by a 0.5 cm long 0.12 T magnetic field, positioned 3.5 cm downstream from the target. A 15 cm  $\times$  10 cm  $\times$  0.8 cm scintillator was placed 26 cm downstream from the slit and was coated with 600-nm thick layer of aluminum to block scatter light.

### Particle pusher simulation

The code simulated the trajectories of electrons by iterating over Eq. 3, where the laser's electric field was calculated using Eqs. 2, and where its out-of-plane magnetic field was given by  $B_z = \frac{1}{k}(\frac{dE_y}{dx} - \frac{dE_x}{dy})$ . In calculating the fields, the laser wavelength, the waist of the incoming Gaussian beam, and the width of the micro-bar were taken to be:  $\lambda = 0.8$   $\mu\text{m}$ ,  $w_{beam} = 3.5$   $\mu\text{m}$  (FWHM), and  $w_{bar} = 2$   $\mu\text{m}$ . The numerical stability of the code was confirmed by inspecting the electron trajectory dependence on  $\Delta t$ . Figure 6 shows the final emission angles of electrons that were simulated on the same conditions as in Fig. 4. The curves show how the integration result stabilizes for  $\Delta t < 5 \times 10^{-4}$  fs, which is the value chosen for the analysis presented in this paper.

### Data availability

The datasets used and/or analysed during the current study available from the corresponding author on reasonable request.

Received: 17 October 2023; Accepted: 30 November 2023

Published online: 04 December 2023

## References

1. Brunel, F. Not-so-resonant, resonant absorption. *Phys. Rev. Lett.* **59**, 52–55 (1987).
2. Thaury, C. & Quéré, F. High-order harmonic and attosecond pulse generation on plasma mirrors: basic mechanisms. *J. Phys. B At. Mol. Opt. Phys.* **43**, 213001 (2010).
3. Passoni, M., Bertagna, L. & Zani, A. Target normal sheath acceleration: Theory, comparison with experiments and future perspectives. *New J. Phys.* **12**, 045012 (2010).
4. Liseykina, T. V., Pirner, S. & Bauer, D. Relativistic attosecond electron bunches from laser-illuminated droplets. *Phys. Rev. Lett.* **104**, 095002. <https://doi.org/10.1103/PHYSREVLETT.104.095002> (2010).
5. Krue, W. L. & Estabrook, K.  $J \times b$  heating by very intense laser light. *The Physics of fluids* **28**, 430–432 (1985).
6. Grimes, M. K., Rundquist, A. R., Lee, Y. S. & Downer, M. C. Experimental identification of “vacuum heating” at femtosecond-laser-irradiated metal surfaces. *Phys. Rev. Lett.* **82**, 4010–4013. <https://doi.org/10.1103/PhysRevLett.82.4010> (1999).
7. Kulcsar, G. *et al.* Intense picosecond X-ray pulses from laser plasmas by use of nanostructured “velvet” targets. *Phys. Rev. Lett.* **84**, 5149 (2000).
8. Samsonova, Z. *et al.* Relativistic interaction of long-wavelength ultrashort laser pulses with nanowires. *Phys. Rev. X* <https://doi.org/10.1103/PhysRevX.9.021029> (2019).
9. Curtis, A. *et al.* Micro-scale fusion in dense relativistic nanowire array plasmas. *Nat. Commun.* **9**, 1077 (2018).
10. Hollinger, R. *et al.* Extreme ionization of heavy atoms in solid-density plasmas by relativistic second-harmonic laser pulses. *Nat. Photonics* **14**, 607–611 (2020).
11. Khaghani, D. *et al.* Enhancing laser-driven proton acceleration by using micro-pillar arrays at high drive energy. *Sci. Rep.* <https://doi.org/10.1038/s41598-017-11589-z> (2017).
12. Zigler, A. *et al.* Enhanced proton acceleration by an ultrashort laser interaction with structured dynamic plasma targets. *Phys. Rev. Lett.* **110**, 215004 (2013).
13. Ebert, T. *et al.* Enhanced brightness of a laser-driven X-ray and particle source by microstructured surfaces of silicon targets. *Phys. Plasmas* **27**, 43106. <https://doi.org/10.1063/1.5125775> (2020).
14. Sumeruk, H. *et al.* Control of strong-laser-field coupling to electrons in solid targets with wavelength-scale spheres. *Phys. Rev. Lett.* **98**, 45001 (2007).
15. Floquet, V. *et al.* Micro-sphere layered targets efficiency in laser driven proton acceleration. *J. Appl. Phys.* **114**, 83305. <https://doi.org/10.1063/1.4819239> (2013).
16. Margarone, D. *et al.* Laser-driven proton acceleration enhancement by nanostructured foils. *Phys. Rev. Lett.* **109**, 234801 (2012).
17. Donnelly, T. D. *et al.* Hard x-ray and hot electron production from intense laser irradiation of wavelength-scale particles. *J. Phys. B At. Mol. Opt. Phys.* **34**, L13 (2001).
18. Fedeli, L. *et al.* Electron acceleration by relativistic surface plasmons in laser-grating interaction. *Phys. Rev. Lett.* **116**, 015001 (2016).
19. Cantono, G. *et al.* Extensive study of electron acceleration by relativistic surface plasmons. *Phys. Plasmas* **25**, (2018).
20. Purvis, M. A. *et al.* Relativistic plasma nanophotonics for ultrahigh energy density physics. *Nat. Photonics* **7**, 796–800 (2013).
21. Born, M. & Wolf, E. *Principles of Optics: Electromagnetic Theory of Propagation, Interference and Diffraction of Light* (Elsevier, Amsterdam, 2013).
22. Cardenas, D. E. *et al.* Sub-cycle dynamics in relativistic nanoplasma acceleration. *Sci. Rep.* **9**, 1–8. <https://doi.org/10.1038/s41598-019-43635-3> (2019).
23. Cardenas, D. *Few Cycle Laser-Driven Electron Accelerators*. Ph.D. thesis, Ludwig Maximilians Universität München (2017).
24. Di Lucchio, L. & Gibbon, P. Relativistic attosecond electron bunch emission from few-cycle laser irradiated nanoscale droplets. *Phys. Rev. Spec. Topics-Accel. Beams* **18**, 023402 (2015).
25. Arber, T. *et al.* Contemporary particle-in-cell approach to laser-plasma modelling. *Plasma Phys. Controlled Fusion* **57**, 113001 (2015).
26. Wang, T., Blackman, D., Chin, K. & Arefiev, A. Effects of simulation dimensionality on laser-driven electron acceleration and photon emission in hollow microchannel targets. *Phys. Rev. E* **104**, 045206. <https://doi.org/10.1103/PHYSREVE.104.045206/FIGURES/8/MEDIUM> (2021).
27. Wilks, S., Krue, W., Tabak, M. & Langdon, A. Absorption of ultra-intense laser pulses. *Phys. Rev. Lett.* **69**, 1383 (1992).
28. Gillen, G. D., Seck, C. M. & Guha, S. Analytical beam propagation model for clipped focused-gaussian beams using vector diffraction theory. *Opt. Express* **18**, 4023–4040 (2010).
29. Porat, E. *et al.* Towards direct-laser-production of relativistic surface harmonics. In *Relativistic Plasma Waves and Particle Beams as Coherent and Incoherent Radiation Sources III*, vol. 11036, 35–40 (SPIE, 2019).
30. Porat, E., Yehuda, H., Cohen, I., Levanon, A. & Pomerantz, I. Diffraction-limited coherent wake emission. *Phys. Rev. Res.* **3**, L032059. <https://doi.org/10.1103/PhysRevResearch.3.L032059> (2021).
31. Pappalardo, A., Cosentino, L. & Finocchiaro, P. An imaging technique for detection and absolute calibration of scintillation light. *Rev. Sci. Instrum.* <https://doi.org/10.1063/1.3360931> (2010).
32. Pomerantz, I. *et al.* Ultrashort Pulsed Neutron Source. *Phys. Rev. Lett.* **113**, 184801 (2014).

## Acknowledgements

We acknowledge aid in target fabrication from the Tel Aviv University Center for Nanoscience and Nanotechnology. Simulations were performed using EPOCH, which was developed as part of the UK Engineering and Physical Sciences Research Council (EPSRC) funded Project No. EP/G054940/1. I.P. acknowledges the support of the Zuckerman STEM Leadership Program. I.P. and S.G acknowledge the support from the National Science Foundation-Binational Science Foundation (NSF no. PHY-1903414; BSF no. 2018641). A.V.A acknowledges the support from the National Science Foundation (No. PHY-1903098) and the National Science Foundation - Czech Science Foundation partnership (NSF award PHY-2206777). This work used HPC resources through allocations 1) PHY190034 from the Advanced Cyberinfrastructure Coordination Ecosystem: Services Support (ACCESS) program, which is supported by National Science Foundation grants #2138259, #2138286, #2138307, #2137603, and #2138296; 2) TG-PHY190034 from the Extreme Science and Engineering Discovery Environment (XSEDE), which is supported by National Science Foundation Grant No. ACI-1548562.

## Author contributions

I.P. and M.E conceptualized and wrote the manuscript, with feedback from all other authors. I.P, A.V.A., and S.H.G obtained funding and supervised this project. M.E. performed and analyzed the experiment, with assistance from I.C., A.L., L.P., and T.C.. M.E and D.B. performed and analyzed the PIC simulations, with assistance from T.M.

### Competing interests

The authors declare no competing interests.

### Additional information

**Supplementary Information** The online version contains supplementary material available at <https://doi.org/10.1038/s41598-023-48866-z>.

**Correspondence** and requests for materials should be addressed to I.P.

**Reprints and permissions information** is available at [www.nature.com/reprints](http://www.nature.com/reprints).

**Publisher's note** Springer Nature remains neutral with regard to jurisdictional claims in published maps and institutional affiliations.



**Open Access** This article is licensed under a Creative Commons Attribution 4.0 International License, which permits use, sharing, adaptation, distribution and reproduction in any medium or format, as long as you give appropriate credit to the original author(s) and the source, provide a link to the Creative Commons licence, and indicate if changes were made. The images or other third party material in this article are included in the article's Creative Commons licence, unless indicated otherwise in a credit line to the material. If material is not included in the article's Creative Commons licence and your intended use is not permitted by statutory regulation or exceeds the permitted use, you will need to obtain permission directly from the copyright holder. To view a copy of this licence, visit <http://creativecommons.org/licenses/by/4.0/>.

© The Author(s) 2023